INSTITUT DE FRANCE
Académie des sciences

# Comptes Rendus

# Physique

Maxime Gay, Minh-Tuan Dau, Céline Vergnaud, Alain Marty, Frédéric Bonell, Hervé Boukari, Colin Paillet, Bérangère Hyot, Hanako Okuno, Pierre Mallet, Jean-Yves Veuillen, Olivier Renault and Matthieu Jamet

**The search for manganese incorporation in $MoSe_2$ monolayer epitaxially grown on graphene**

Volume 22, Special Issue S4 (2021), p. 5-21

Published online: 3 May 2021
Issue date: 8 March 2022

https://doi.org/10.5802/crphys.69

**Part of Special Issue:** Recent advances in 2D material physics
**Guest editors:** Xavier Marie (INSA Toulouse, Université Toulouse III Paul Sabatier, CNRS, France) and Johann Coraux (Institut Néel, Université Grenoble Alpes, CNRS, France)



*Les* Comptes Rendus. Physique *sont membres du Centre Mersenne pour l'édition scientifique ouverte*
www.centre-mersenne.org
e-ISSN : 1878-1535

*Comptes Rendus*
*Physique*
**2021**, 22, nº S4, p. 5-21
https://doi.org/10.5802/crphys.69

Recent advances in 2D material physics / *Physique des matériaux bidimensionnels*

# The search for manganese incorporation in $MoSe_2$ monolayer epitaxially grown on graphene

**Maxime Gay [a], Minh-Tuan Dau [b], Céline Vergnaud [b], Alain Marty [b], Frédéric Bonell [b], Hervé Boukari [c], Colin Paillet [a], Bérangère Hyot [a], Hanako Okuno [d], Pierre Mallet [c], Jean-Yves Veuillen [c], Olivier Renault [a] and Matthieu Jamet [*, b]**

[a] Univ. Grenoble Alpes, CEA, Leti, F-38000 Grenoble, France

[b] Univ. Grenoble Alpes, CEA, CNRS, Spintec, F-38000 Grenoble, France

[c] Univ. Grenoble Alpes, CNRS, Institut Néel, F-38000 Grenoble, France

[d] Univ. Grenoble Alpes, CEA, IRIG-MEM, F-38000 Grenoble, France

*E-mails:* maxime.gay@protonmail.com (M. Gay), dautuan@gmail.com (M.-T. Dau), celine.vergnaud@cea.fr (C. Vergnaud), alain.marty@cea.fr (A. Marty), frederic.bonell@cea.fr (F. Bonell), herve.boukari@cea.fr (H. Boukari), colin.paillet@cea.fr (C. Paillet), berangere.hyot@cea.fr (B. Hyot), hanako.okuno@cea.fr (H. Okuno), pierre.mallet@neel.cnrs.fr (P. Mallet), jean-yves.veuillen@neel.cnrs.fr (J.-Y. Veuillen), olivier.renault@cea.fr (O. Renault), matthieu.jamet@cea.fr (M. Jamet)

**Abstract.** The introduction of magnetism in two-dimensional (2D) materials represents an intense field of research nowadays and the quest to reach above-room-temperature ordering temperatures is still underway. Intrinsic ferromagnetism was discovered in 2017 in $CrI_3$ and $Cr_2Ge_2Te_6$ in the monolayer form with low Curie temperatures. An alternative method to introduce magnetism into conventional 2D materials is substitutional doping with magnetic impurities similarly to three-dimensional diluted magnetic semiconductors. The case of Mn-doped transition metal dichalcogenide ($MoS_2$, $MoSe_2$, $WS_2$, $WSe_2$) monolayers is very interesting because combining out-of-plane ferromagnetism and valley contrast leads to ferrovalley materials. In this work, we focus on the incorporation of Mn in $MoSe_2$ by molecular beam epitaxy on graphene which has been rarely addressed up to now. By using a multiscale characterization approach, we demonstrate that Mn atoms are incorporated into the $MoSe_2$ monolayer up to 5 atomic percent. However, when incorporated into the film, Mn atoms tend to diffuse to the grain edges forming undefined $Mo_xMn_ySe_z$ phase at grain boundaries after completion of the $MoSe_2$ monolayer. This segregation leaves the crystalline and electronic structure of $MoSe_2$ unmodified. Above 5%, the saturation of Mn content in $MoSe_2$ leads to the formation of epitaxial MnSe clusters.

**Keywords.** 2D materials, Magnetic doping, Molecular beam epitaxy, Transmission electron microscopy, Scanning tunneling microscopy, Momentum resolved photoemission electron microscopy.

Available online 3rd May 2021

[*] Corresponding author.

## 1. Introduction

Spintronics aims at exploiting the spin degree of freedom of electrons and led to very important achievements in data storage and sensor industries [1]. To date, only ferromagnetic metals were used in elementary devices like spin valves or magnetic tunnel junctions preventing easy electrical control of magnetic properties. The emergence of dilute magnetic semiconductors (DMS) where ferromagnetism is mediated by charge carriers offered the opportunity to electrically control their magnetic properties [2]. For instance, the Curie temperature [3] and magnetic anisotropy [4] of Mn-doped GaAs could be tuned by applying an electric field. However, those materials still suffer today from low Curie temperatures [5] and remain difficult to stabilize due to the very low solubility of magnetic impurities like Mn in conventional semiconductors like GaAs, GaN or Ge [6].

In parallel, the field of 2D semiconductors like transition metal dichalcogenides (TMD) of formula $MX_2$ (M = Mo, W and X = S, Se) and others has grown considerably in the last decade for their exceptional optical and electrical properties [7,8]. In order to turn these materials magnetic, it is natural to explore the incorporation of magnetic atoms like Mn which exhibits the largest spin moment among transition metals. Molecular beam epitaxy (MBE) has been the principal tool to grow DMS [9]. Due to the lack of lattice matched substrates, the method to grow epitaxial TMD monolayers either by MBE or chemical vapor deposition is the van der Waals (vdW) epitaxy [10]. In this regime, the weak vdW interaction between the substrate and the TMD releases the lattice matching constraint and makes possible the growth of fully relaxed TMD monolayers. If the substrate is single crystalline, the weak vdW interaction is sufficient to ensure the epitaxial growth of the TMD and obtain good crystalline quality. The substrates are usually vdW materials like graphene [11, 12] or mica [13, 14] but passivated surfaces like Se-passivated GaAs also give very good epitaxial growths [15, 16].

To date, Mn doping has been little investigated in TMD monolayers. Early theoretical work predicted long-range ferromagnetism in Mn-doped TMD monolayers [17]. When Mn substitutes Mo or W and for concentrations less than 5%, the ferromagnetic coupling between Mn spins is mediated by the antiferromagnetic exchange interaction between the localized $d$ states of Mn and the delocalized $p$ states of chalcogen atoms. In $MoSe_2$, Mn atoms are expected to carry a spin moment of $1.27\mu_B$ and introduce gap states close to the Fermi level and at the bottom of the conduction band. However very few experimental achievements have been reported so far [13, 18–20]. In Ref. [19], the authors raised an important issue related to the high reactivity of Mn atoms. During growth, when Mn atoms or precursors are in direct contact with the $SiO_2$ substrate, they tend to react with oxygen atoms and not to incorporate into $MoS_2$. The use of a vdW substrate like graphene is more suitable to achieve Mn doping. In Ref. [20], the authors developed another growth method on $SiO_2$ called solid phase epitaxy where Mn atoms are not in direct contact with the $SiO_2$ substrate. It allows the incorporation of Mn atoms into $MoSe_2$ without evidence of Mn clustering. However the exact position of Mn atoms in $MoSe_2$ could not be resolved. In Refs. [20] and [19], the authors do not provide magnetic measurements and there is no direct proof of efficient magnetic doping and ferromagnetism in Mn doped $MoS_2$ and $MoSe_2$. In contrast, in Refs. [13] and [18], the authors report temperature dependent magnetic measurements of Mn doped $MoSe_2$ multilayers grown on mica and Mn doped $MoS_2$ nanostructures respectively. As long as parasitic magnetic signals from the substrate can be neglected, the authors observe the coexistence of a strong paramagnetic signal at low temperature and a very soft ferromagnetic signal persisting up to 100 K. However, in both works, Mn atoms could not be accurately located in $MoSe_2$ and $MoS_2$ probably because it is challenging from a technical point of view. Hence, the exact origin of ferromagnetism is not clearly stated. It can originate from substitutional doping of Mn atoms or to any Mn-rich phase in the form of $Mo_xMn_ySe_z$ or $Mo_xMn_yS_z$ due to Mn segregation.

In this work, we study the MBE growth of $Mo_{1-x}Mn_xSe_2$ monolayers by co-evaporating all three elements in ultra high vacuum (UHV) conditions on a graphene substrate. By using a multiscale characterization approach, we conclude that the Mn solubility in $MoSe_2$ monolayer is extremely low. In optimized growth conditions for $MoSe_2$, Mn atoms spontaneously segregate at the $MoSe_2$ grain edges during the growth forming an undefined $Mo_xMn_ySe_z$ phase at grain boundaries. As a consequence, the crystal and electronic structures of $MoSe_2$ are almost unaffected by the incorporation of Mn atoms. Moreover, above 5%, $\alpha$-MnSe(111) clusters appear at the surface of the film.

## 2. Sample growth and crystal structure

$Mo_{1-x}Mn_xSe_2$ monolayers were grown by MBE on a graphitized 6H-SiC(0001) substrate in a UHV chamber with a base pressure of $5 \times 10^{-10}$ mbar. For scanning transmission electron microscopy (STEM) observations, the films were deposited in the same conditions on a graphene layer grown by CVD on platinum which allows for their transfer on TEM grids by an electrochemical method [21]. The CVD graphene on platinum is polycrystalline with 10 µm-large single-crystalline domains. We assume that, in the middle of a domain, the growth proceeds the same as on epitaxial graphene on SiC. This assumption is reasonable since the graphene layer is screening the substrate underneath and the surface chemistry (which is critical for the growth and Mn incorporation) is of van der Waals type in both cases.

Before the growth, the substrate was thermally cleaned in the MBE chamber at a temperature of 750 °C for 15 min. The growth temperature was 500 °C. Molybdenum and selenium are respectively evaporated by an electron gun evaporator and an effusion cell. The direct Se flux measured at the sample position using a retractable Bayard–Alpert gauge was between $1 \times 10^{-6}$ and $2 \times 10^{-6}$ mbar. The Mo deposition rate, measured with a quartz balance, was 1.1 Å/min. Note that these growth conditions (temperature and depostion rates) were optimized to obtain the best crystalline quality of $MoSe_2$ monolayers on graphene.

Considering the low Mn concentrations (<10%), manganese cannot be incorporated during the whole duration of the $MoSe_2$ monolayer growth because the required flux would be too low to be under control. Here, Mn is evaporated with an electron gun evaporator at a stable rate of 0.75 Å/min. We thus used a sequential incorporation of manganese (typically in 2 or 3 times regularly spaced in time) during the growth of $MoSe_2$. We studied six different $Mo_{1-x}Mn_xSe_2$ samples with compositions $x = 0$; 0.01; 0.025; 0.05; 0.075 and 0.1 respectively. The Mn content was calibrated by Rutherford Backscattering measurements [13]. Post-growth annealing was performed at 750 °C during 15 min under Se flux to improve the crystalline quality [21]. Finally, the as-grown monolayers were coated by a 15 nm-thick amorphous Se protecting layer to avoid their oxidation in air during their transfer to the characterization techniques except for transmission electron microscopy.

The crystal structure of $Mo_{1-x}Mn_xSe_2$ monolayers was monitored in-situ by Reflection High Energy Electron Diffraction (RHEED). The different RHEED patterns obtained for the 6 samples are displayed in Figure 1. They clearly exhibit an anisotropic character with different patterns along the [100] and [110] crystal directions. Considering the initial RHEED pattern of graphene also shown in Figure 1, we can conclude that the $Mo_{1-x}Mn_xSe_2$ monolayers are all in epitaxial relationship with graphene regardless the Mn concentration. Moreover, RHEED patterns only exhibit thin streaks up to 2.5% of Mn. Bright spots (highlighted by white arrows in Figure 1) appear in the RHEED patterns for Mn compositions of 5% and above. From the lateral position of the spots compared to the one of $MoSe_2$ streaks, we deduce a lattice spacing of 3.85 Å. It corresponds to the interplanar distance of the cubic phase of MnSe shown in Figure 2a.

As shown in Figure 2b, the position of the diffraction spots can be well explained by the presence of cubic MnSe clusters at the surface of $MoSe_2$ or bare graphene with (111)

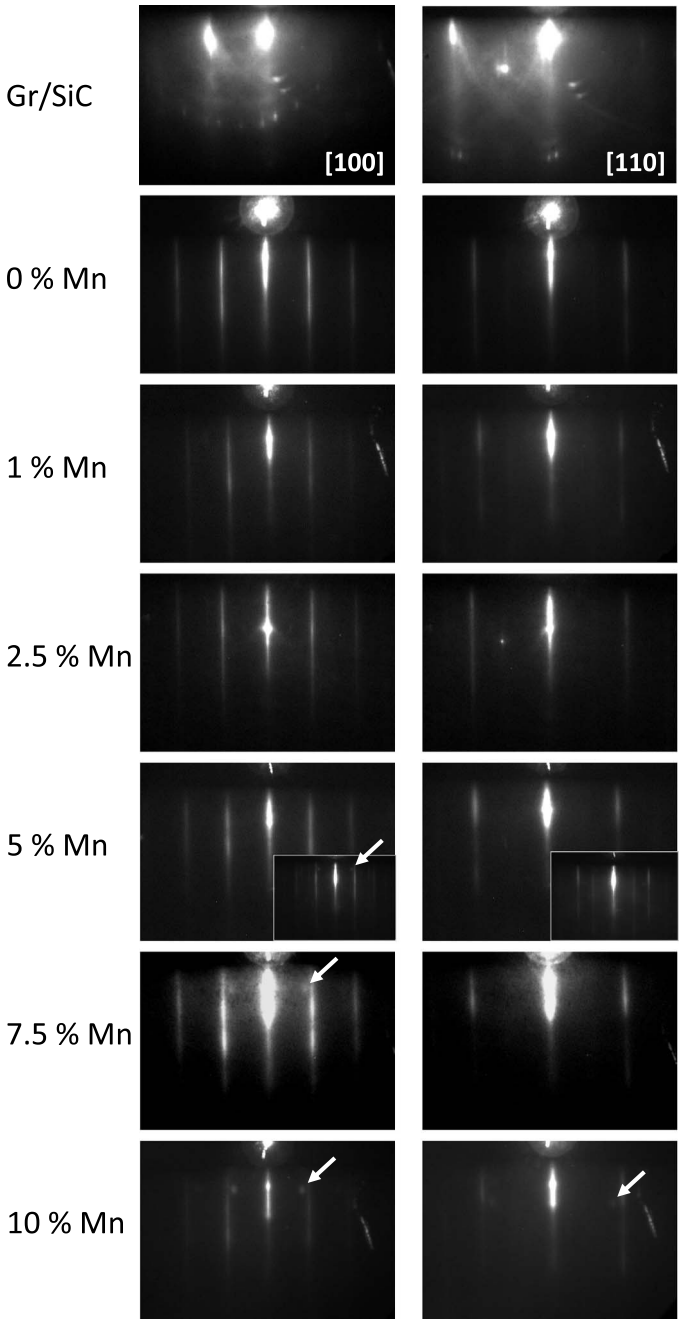


**Figure 1.** RHEED patterns recorded along two different azimuths [100] and [110] for the graphene substrate and different Mn concentrations (from top to bottom): 0%; 1%; 2.5%; 5%; 7.5% and 10%. The RHEED patterns were recorded at room temperature after thermal cleaning for the substrate and after the post-growth annealing for $Mo_{1-x}Mn_xSe_2$ monolayers. White arrows point to bright spots in the RHEED patterns. For 5% Mn, the insets show RHEED patterns for the electron beam in grazing incidence.

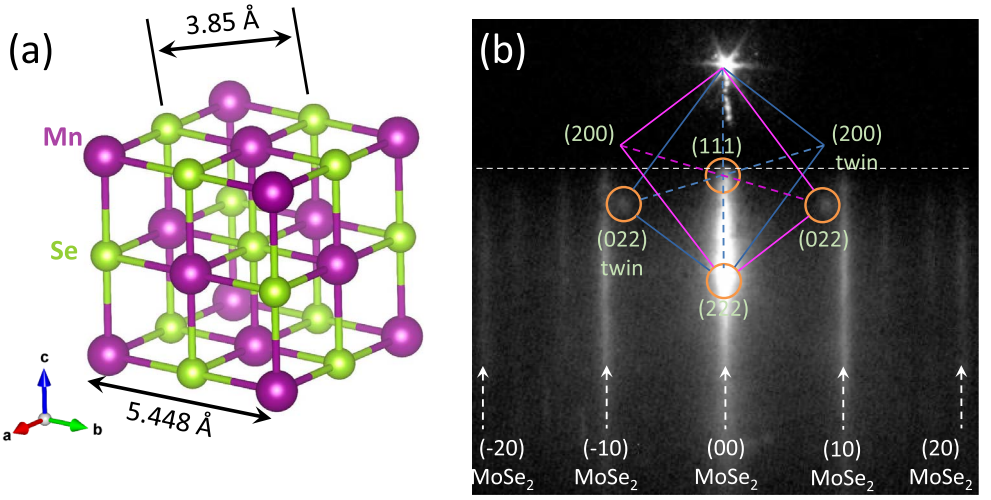


**Figure 2.** (a) Ball-and-stick representation of the cubic MnSe crystal. (b) RHEED pattern of a $MoSe_2$ monolayer doped with 10% of Mn along the [100] crystal axis. We use a grazing incidence electron beam in order to observe the diffraction spots circled in orange in the figure. The blue and purple rectangles with the associated (111); (222); (022) and (200) nodes correspond to the reciprocal lattice of two twin MnSe clusters at the surface of $MoSe_2$ with opposite in-plane crystal orientations.

orientation. From the RHEED patterns, their epitaxial relationship with $MoSe_2$ (resp. graphene) is $MnSe(4\bar{2}\bar{2})||MoSe_2(100)$ (resp. Gr(100)). The presence of twin MnSe clusters on $MoSe_2$ is due to the presence of $MoSe_2$ twin grains as expected for the epitaxial growth of $MoSe_2$ on graphene [21, 22]. The presence of twin MnSe clusters on graphene is also expected due to the six-fold symmetry of the graphene surface.

Grazing incidence X-ray diffraction measurements were performed using a SmartLab Rigaku diffractometer equipped with a copper rotating anode beam tube ($\lambda_{K_\alpha}$ = 1.54 Å) and operated at 45 kV and 200 mA. A parabolic mirror and a parallel in-plane collimator with a 0.5° resolution was used in the primary optics and a second parallel collimator was used in the secondary one. Parasitic radiations were eliminated by a $K_\beta$ filter inserted on the detector side. The results are shown in Figure 3 for 3 different Mn concentrations: 0%; 2.5% and 5%. All the measurements were done with the selenium capping on top.

According to the radial scans along the SiC(h00) direction in Figure 3a and along the SiC(hh0) direction in Figure 3b, the incorporation of Mn up to a concentration of 5% does not affect the $MoSe_2$ crystal structure. The (100), (110) and (200) Bragg peaks of $MoSe_2$ remain unchanged when increasing the Mn content. In the same way, the azimutal scans of the $MoSe_2$(110) Bragg peak in Figure 3c show that the mosaic spread of $MoSe_2$ grains is unaffected by the incorporation of Mn. It remains in the 6°–8° range. In the 5% Mn sample, we could not detect the presence of MnSe by X-ray diffraction which might be due to the small size of the MnSe clusters at the sample surface as shown by STEM in the following.

## 3. Atomic scale analysis of Mn-doped $MoSe_2$

### 3.1. *Scanning transmission electron microscopy*

After their transfer on a TEM grid, $Mo_{1-x}Mn_xSe_2$ monolayers are observed by angular dark field scanning transmission electron microscopy (ADF-STEM). STEM measurements have been

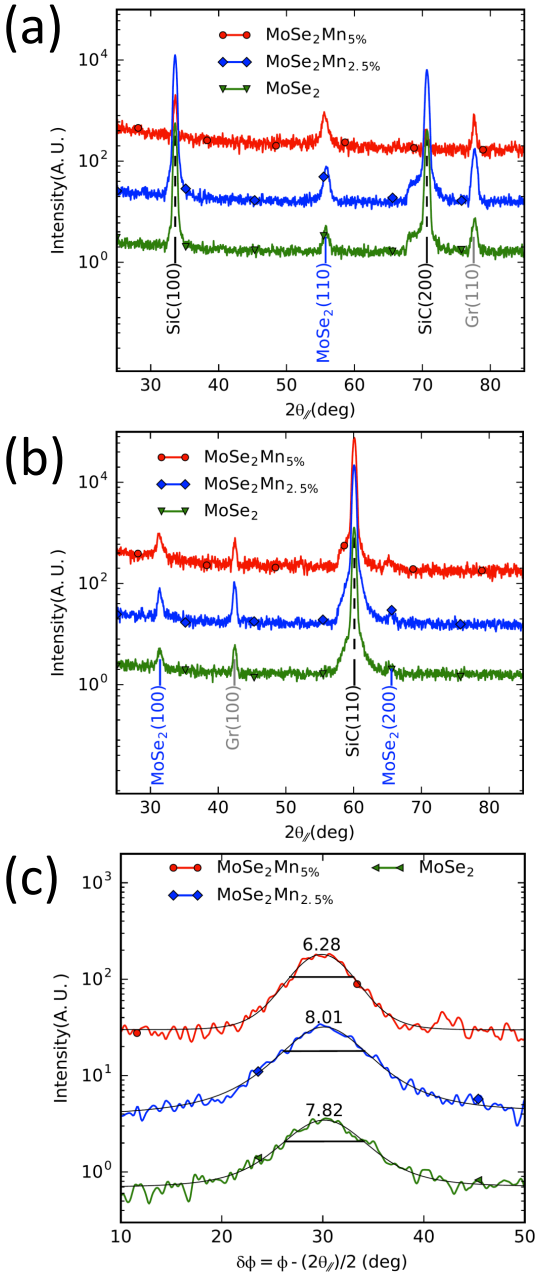


**Figure 3.** Grazing incidence X-ray diffraction spectra for 0%; 2.5% and 5% of Mn. (a) Radial scans along the SiC(h00) direction and (b) along the SiC(hh0) direction. (c) Azimutal scans around the (110) $MoSe_2$ Bragg peak for 0%; 2.5% and 5% of Mn. The solid black lines are fits giving the full width at half maximum (FWHM) of the peaks i.e. the mosaic spread of $MoSe_2$ grains.

carried out using a double Cs-corrected FEI Ultimate at 80 kV. ADF-STEM images were acquired using a convergence semi-angle of 22 mrad and collecting scattering larger than 50 mrad. Here, we stress the fact that we observe by ADF-STEM the same epitaxial relationship between CVD

graphene and $MoSe_2$ lattices as the one between epitaxial graphene on SiC and $MoSe_2$ lattices observed by RHEED and X-ray diffraction in Section 2 and by $k$-PEEM in Section 4.2.

We first focus on the sample containing 1% of Mn. Low and high magnitude STEM images of this sample are shown in Figures 4a and 4b respectively. We observe the nearly completion of the $MoSe_2$ monolayer in dark grey. Black and light grey areas correspond to uncovered graphene and to the second $MoSe_2$ monolayer respectively. In Figure 4b, we note the presence of dark spots at Se sites which correspond to Se vacancies. The atomic details are shown in the $Z$-contrast ($Z$ being the atomic number) image of Figure 4c. Mo, Se and Se vacancy sites are clearly identified in the intensity profile of Figure 4e by their relative $Z$-contrast. The creation of Se vacancies is a known effect due to electron irradiation during the STEM observations. As the amount of Se vacancies observed in this sample containing Mn was equivalent to that routinely observed in undoped samples, we consider that there is no impact of Mn doping on Se sites.

STEM observations at several positions on the sample did not show the presence of clusters at the surface of the sample. Moreover a thorough analysis in the inner parts of $MoSe_2$ single crystalline grains did not show the presence of Mn atoms in substitution of Mo except one shown in the $Z$-contrast image of Figure 4d. In the intensity profile of Figure 4f, the relative $Z$-contrast at each atomic position allowed us to detect the presence of one impurity atom substituting Mo, supposed to be a Mn atom according to its relative intensity.

A second sample containing 5% of Mn was also studied by STEM and the results are shown in Figure 5. In Figure 5a and b, the low and high magnitude STEM images exhibit several features. First, we find again the nearly completion of one $MoSe_2$ monolayer in dark grey. Black and light grey areas correspond to uncovered graphene and to the second $MoSe_2$ monolayer respectively. In this sample, we also observe a high density of nanoparticles at the surface of $MoSe_2$.

In Figure 5a, nanoparticles have a diameter of 10 to 20 nm and in Figure 5b, smaller nanoparticles with a diameter of 1 nm can be detected. Those nanoparticles correspond to MnSe clusters also detected by RHEED in the $Mo_{0.95}Mn_{0.05}Se_2$ sample. This is confirmed by the electron energy loss spectroscopy (EELS) map at the Mn L-edge shown in Figure 5c: all the clusters are Mn-rich. However, since the STEM sample was not capped with amorphous selenium, the MnSe clusters are fully oxidized as demonstrated by the elemental EELS map at the O K-edge in Figure 5d. Again, it was not possible to detect Mn atoms substituting Mo in $MoSe_2$ single crystalline domains.

### 3.2. *Scanning tunneling microscopy and spectroscopy*

In order to elucidate the position of Mn atoms, we have analyzed by STM/STS at 8 K two similar samples with a nominal Mn doping level of 5% Mn. The $MoSe_2$ coverage was around 1 ML and the amorphous selenium coating layer was first removed in vacuum by a soft annealing at around 200°. Compared to the case of undoped (bare) $MoSe_2$ layers grown using the same technique and growth conditions [11,23], large scale images (not shown) reveal two kinds of parasitic structures in the Mn doped samples. The first one is a sparse distribution of small three-dimensional grains with a typical height of 3 nm corresponding to the MnSe clusters detected by RHEED and STEM. The second one consists in small patches (a few nanometers in lateral size) of a two-dimensional unidentified phase attached to the semiconducting $MoSe_2$ islands. Its apparent height is 0.4 nm, much smaller than the one measured on semiconducting $MoSe_2$ monolayer islands (0.7–0.8 nm). We shall not discuss these structures in this section, which is devoted to the Mn doping of the semiconducting 2H TMD. We simply notice that these phases (clusters and patches) may incorporate a significant amount of the deposited Mn, which would naturally explain the discrepancy between the rather high nominal Mn doping of the TMD layer and the fairly low concentration of Mn found in the TMD flakes as shown in the following. We recall that a homogeneous doping of 2H-$MoSe_2$ by 5% should result in a mean spacing of ≈1.5 nm between Mn atoms.

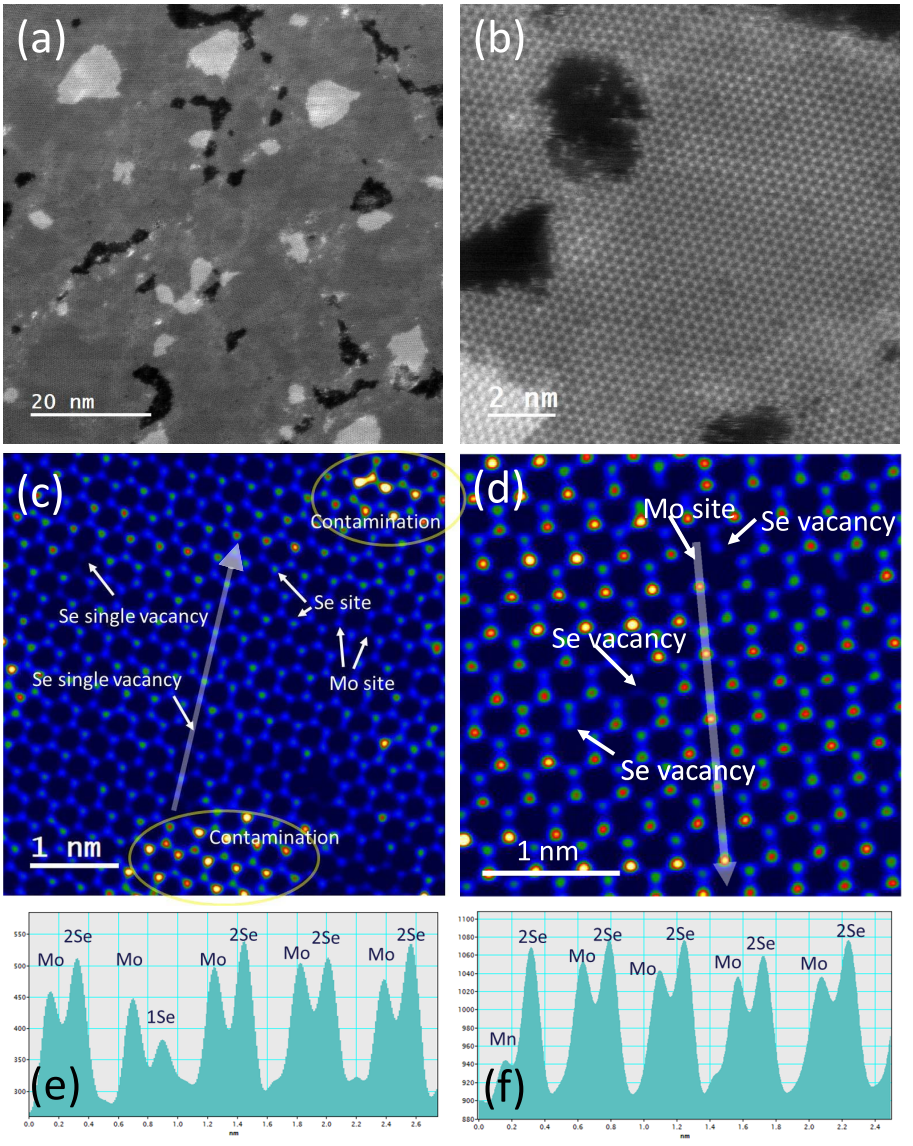


**Figure 4.** (a) Low and (b) high magnitude TEM images of the $Mo_{0.99}Mn_{0.01}Se_2$ sample. The black, dark grey and light grey contrasts correspond to zero, one and two $MoSe_2$ monolayers respectively. The dark spots in (b) are mostly due to Se vacancies. (c) Low and (d) high magnitude STEM images showing several features: Mo and Se sites; Se vacancies and contaminated areas. (e) and (f) correspond to the intensity profiles along the white arrow in (c) and (d) respectively.

Figure 6a is an overview of a TMD flake for the doped sample. The morphology of the flakes is indeed quite similar to the one observed in undoped layers [11, 23]. The monolayer of $MoSe_2$ (1L-$MoSe_2$) island has a shape approximately triangular. A second layer (2L-$MoSe_2$) grows on top of the first layer. In both layers we observe the characteristic triangular pattern of mirror twin boundaries (TB) which have been studied previously by STM/STS [24, 25]. Actually, the only difference we can see with bare $MoSe_2$ samples is the presence of atomic size features which

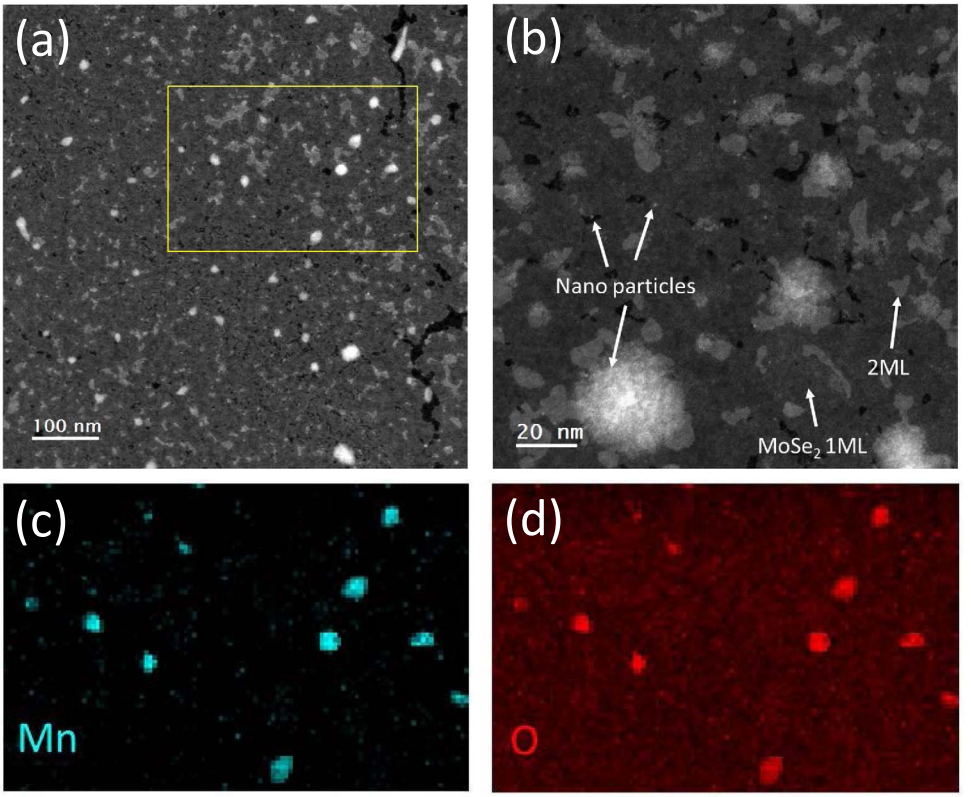


**Figure 5.** (a) Low and (b) high magnitude STEM images of the $Mo_{0.95}Mn_{0.05}Se_2$ sample. The black, dark grey and light grey contrasts correspond to zero, one and two $MoSe_2$ monolayers respectively. The bright dots correspond to small nanometer sized clusters. (c) and (d) Electron energy loss spectroscopy (EELS) in the zone delimited by the yellow rectangle in (a) recorded at the Mn L-edge and O K-edge respectively showing that the clusters are Mn-rich and oxidized in air.

accumulate close to the edges (and grain boundaries as well) and decorate the 1L-$MoSe_2$ grains. Some of these accumulation areas are indicated by the green ellipses in Figure 6a. Similar features are observed on 2L-$MoSe_2$, which are occasionally found farther apart from the edges (blue ellipse in Figure 6a).

Figure 6b and c present images taken at positive and negative biases of the same area on another 1L-$MoSe_2$ flake. With these biases, we probe electronic states located close to the bottom of the conduction band and to the top of the valence band of (bulk) 1L-$MoSe_2$ in Figures 6b and 6c respectively. In the two images, we can see objects with sub-nanometer sizes (examples are indicated by the green ellipse) along the edges of the flake. All these structures exhibit a similar contrast (apparent height and size) for the two biases shown in Figure 6b and c, and more generally for all the different biases we have used in the measurements (typically from +1.2 V to −2.3 V). This indicates that all these objects have the same origin. Since they were not observed in bare $MoSe_2$ samples, we ascribe the structures (some of them circled in green) shown in Figure 6b and c to Mn atoms incorporated in the TMD matrix. Note that inside the flake, more than 5 nm away from the edges, the TMD seems to be quite homogeneous (except for the unavoidable TB). This homogeneous contrast in the interior of the 1L-$MoSe_2$ was verified at different positions

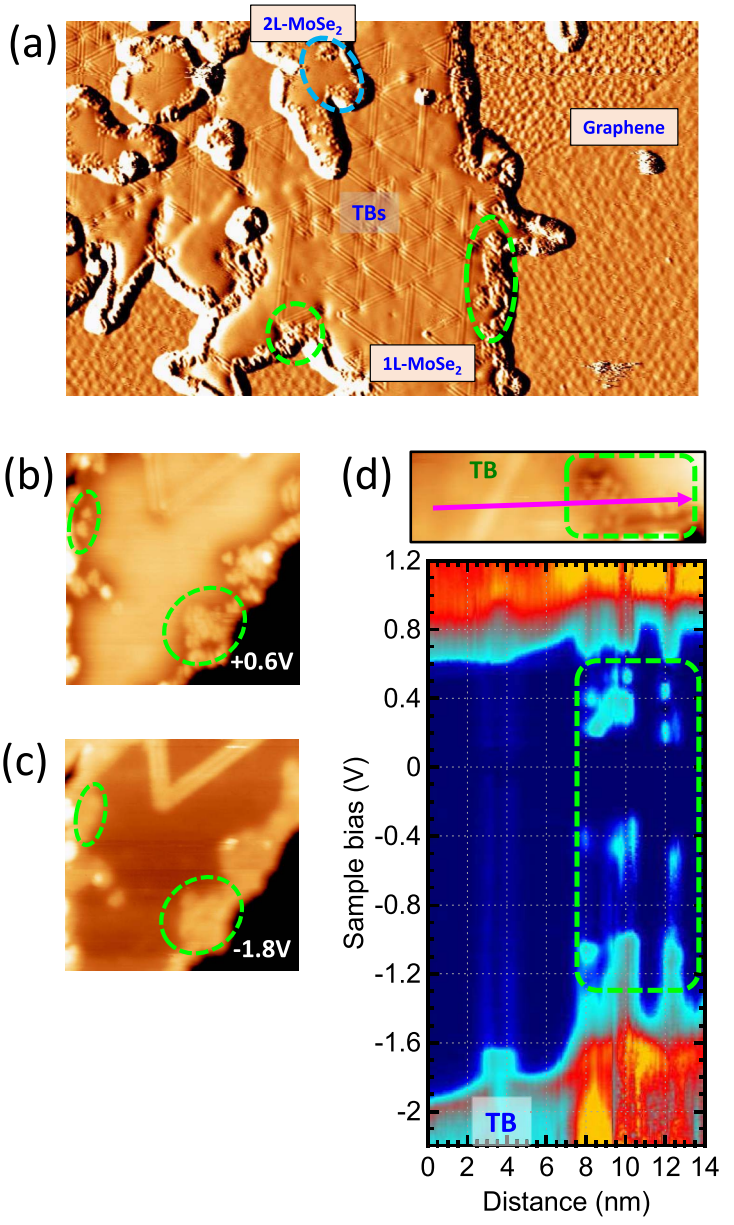


**Figure 6.** Characterization of the Mn doped $MoSe_2$ samples by STM/STS. (a) STM image (size: $100 \times 60$ nm$^2$, sample bias: +1.0 V) in the derivative ($dz/dx$) mode of a TMD flake. The ellipses indicate areas where Mn related features were identified. Mirror Twin Boundaries (TB) lines are also identified in the TMD flake. (b) and (c) STM images (on another flake) of the same area with a size of $28 \times 28$ nm$^2$ taken at sample biases of +0.6 V and −1.8 V respectively. The green ellipses highlight structures identified as Mn dopants. (d) Top: STM image (size: $16 \times 5$ nm$^2$, sample bias: +1.2 V) of a 1L-$MoSe_2$ flake edge where several Mn atoms are located in the area enclosed by the green box. The flake edge shows up at the bottom right corner of the image. Bottom: Conductance map $dI/dV(x, V)$ recorded along the 14 nm-long pink line in the top panel. The distance between each spectra is 118 pm. The set point conditions for the spectra are a sample bias of +1.2 V and current 400 pA.

and using different biases. This is in good agreement with ADF-STEM observations in the middle of CVD graphene domains far from grain boundaries. It supports the fact that the MBE growth of $Mo_{1-x}Mn_xSe_2$ on CVD graphene and epitaxial graphene on SiC are similar. In the same way, we found exactly the same result in vanadium doped $WSe_2$ [26] where STM and ADF-STEM observations are also comparable in the middle of graphene grains.

From our own experience and from published works, we know that variable bias imaging allows for the detection of isoelectronic substitutional atoms in TMD layers, such as O on S/Se sites [27] or Mo on W sites [28,29]. We expect that the incorporation of non-isoelectronic dopants such as Mn in $MoSe_2$, would give rise to a larger perturbation in the local electronic structure of the TMD matrix, and thus to a contrast (on the nanometer size) that should be easily observed using STM, as recently achieved in $WSe_2$ flakes doped with V atoms [26]. The presence of such a contrast at the edge and its absence inside the island suggests that Mn atoms are only present close to the boundaries of the flakes.

The fact that Mn atoms are only present close to the edges of 1L-$MoSe_2$, and that they tend to accumulate there, is not favorable for STS studies. Indeed, it is difficult to extract from these data information about the electronic structure of isolated Mn atoms in a $MoSe_2$ matrix, which is the situation considered in theoretical studies [17, 30–32]. It is known [33, 34] that there is a strong upwards band bending which develops at the edges of semiconducting TMD layers deposited on graphene (or graphite). This band bending of typically 300 meV extends 5 nm away from the edge for bare $MoSe_2$ [34]; it corresponds to the area where Mn dopants accumulate. As a consequence, the location (in energy) of the valence and conduction band edges at the defect site are quite uncertain. In addition, in-gap edge states (which eventually pin the Fermi level) are observed at the boundaries of bare semiconducting TMDs [33, 34]. Despite these limitations, we have nevertheless performed STS studies on several Mn agglomerates on 1L and 2L-$MoSe_2$ layers. One example is shown in Figure 6d for a Mn agglomerate in a 1L-$MoSe_2$ flake. We have taken a series of spectra along the pink line in the top panel. This line starts on a clean $MoSe_2$ area. It first crosses a TB, and then enters the agglomerate highlighted with the green box. The conductance map obtained from this series of spectra is displayed in the bottom panel of Figure 6d. The dark blue area corresponds to the bandgap of the $MoSe_2$ layer. The TB gives a significant density of states within this bandgap as expected [24, 25]. For distances between 5 and 7 nm, a strong upwards band bending is seen when approaching the Mn agglomerate. On the Mn agglomerate (green boxed area), we see a set of discrete in-gap states, located on both sides of the Fermi level $E_F$ (here $E_F$ corresponds to zero sample bias). The highest occupied (lowest empty) in-gap states are located at $-0.4$ eV below ($+0.2$ eV above) $E_F$ respectively. We find that Mn dopants generally give rise to both occupied and empty in-gap states (with different binding energies depending on the local configurations) for the different areas we have probed by STS. Such in-gap states both in occupied and empty states are actually predicted by ab-initio calculations [17, 30–32]. However, for the reasons quoted above, those STS results may not be directly compared with such calculations.

## 4. Electronic structure

### 4.1. *X-ray photoemission spectroscopy*

XPS measurements were performed under ultrahigh vacuum with an X-ray microprobe (beam size of 100 μm) photoelectron spectrometer (PHI 5000 VersaProbe-II) fitted with a monochromatic Al $K_\alpha$ source ($h\nu$ = 1486.7 eV). The photoelectron take-off angle was 45° and the overall energy resolution 0.6 eV for high resolution core level spectra. The C 1s peak, commonly used for energy referencing, overlaps with a Se Auger line and becomes hard to identify when the sample is poorly covered by adventitious carbon [35]. Therefore the energy scale was calibrated

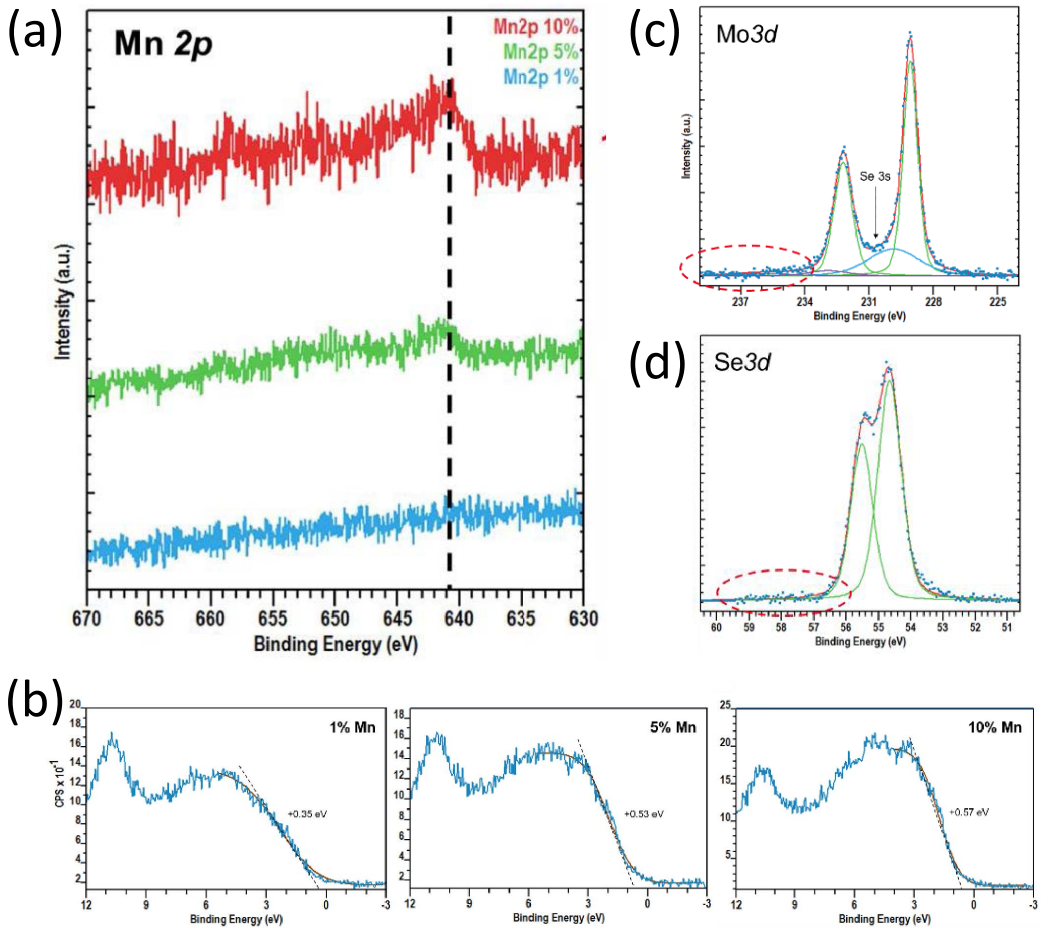


**Figure 7.** (a) Mn 2p core-level and (b) valence band spectra for $Mo_{1-x}Mn_xSe_2$ samples with $x = 0.01$; 0.05 and 0.1. (c) Mo 3d and (d) Se 3d core-level spectra for the sample containing 5% of Mn. Solid lines are fits.

by shifting the Si 2p peak, coming from the SiC substrate. The decomposition of the core-level line shape into individual bonding-state components was done with the CasaXPS software, using the sum of 30% Lorentzian and 70% Gaussian line-shapes and Shirley background subtraction. The spin-orbit splitting was set to 3.1 eV for Mo 3d, 0.9 eV for Se 3d and 11.5 eV for Mn 2p. In the particular case of Mn 2p, we considered a Lorentzian asymmetric line-shape according to Ref. [36] and a linear background due to a poor peak intensity caused by a low photoionization cross section [37] and a small amount of atoms combined with a strong inelastic background from the nearby Se Auger lines.

Prior to the XPS analysis, the samples were heated at 350 °C under UHV in order to remove the Se capping layer and leave a clean surface suitable for the measurements. Figure 7a shows the series of Mn 2p spectra with increasing doping concentration. The series of corresponding valence band spectra is presented in Figure 7b. The Mo 3d and Se 3d core-level spectra of the 5% Mn doped sample are displayed in Figures 7c and 7d respectively. The red-dashed ellipses point out the absence of Mo or Se oxide in the sample as expected from the preparation protocol. The Mo and Se binding energies are compatible with previous results on $MoSe_2$ monolayers [20]. The

series of Mn spectra shows an increased Mn 2p intensity upon increasing nominal concentration, evidencing that the effective Mn incorporation within the $MoSe_2$ layer keeps on increasing when increasing the initial Mn content. The Mn $2p_{3/2}$ main peak corresponds to a 641 eV binding energy i.e. 2 eV larger than for metallic Mn which is indicative of oxidized Mn. Since oxygen is not found in the survey spectra (not shown), and Se has a higher electronegativity than Mn, we can conclude that at least a significant fraction of Mn is incorporated in the form of MnSe compounds. The series of valence band spectra, which reveals a monotonic shift of the valence band maximum away from the Fermi level upon increasing of the nominal Mn concentration (from 0.35 up to 0.57 eV for 1% to 10% Mn doping, respectively). This shift is equivalent to n-type doping or more generally, can be attributed to the occupation of additional electronic states in the bandgap of $MoSe_2$ at room temperature. However, n-type doping of $MoSe_2$ can be ruled out since we do not observe a clear rigid shift of Mo 3d and Se 3d core-level spectra towards lower binding energies as expected upon n-type doping. The electronic states responsible for the shift of the valence band maximum may thus originate from another phase than $MoSe_2$ present in the sample as shown in the following.

### 4.2. *k-resolved photoemission electron microscopy*

The *k*-PEEM analysis was performed using a NanoESCA MkI spectro-microscope (ScientaOmicron) [38, 39] in ultra-high vacuum conditions and at ambient temperature. A He-I cold cathode lamp ($h\nu = 21.1$ eV) was used as a laboratory, vacuum-ultra-violet (VUV) excitation source impinging the sample in an off-normal direction, namely at an angle of 65° with respect to the sample normal. Momentum-resolved images were acquired over the first Brillouin zone ($k_x, k_y = \pm 1.8$ Å$^{-1}$). The high energy resolution momentum images were recorded at a spectrometer pass energy of 50 eV and a 1 mm diameter entrance slit of the imaging spectrometer (equivalent to an overall energy resolution of ≈0.2 eV), and with low-noise, event-counting detection allowing enhanced sensitivity for precise upper valence band analysis. The calibration of the *k*-space scale was done by measuring the known reciprocal lattice distances of a freshly prepared Cu(111) single crystal surface with identical PEEM settings as applied to the $MoSe_2$ samples.

Figure 8a shows the angular image of the 1-ML $MoSe_2$ sample containing 5% of Mn recorded at a binding energy of 1.58 eV. It shows the K points of both $MoSe_2$ and graphene layers which are perfectly aligned confirming the epitaxial growth of the $MoSe_2$ monolayer on graphene. The full band structure was then generated from the series of angular images recorded from −0.5 to 5 eV binding energies. Figure 8b shows a cut along the K–Γ–K′ direction. The band structure clearly shows the monolayer character of the doped $MoSe_2$ layer, with the valence band maximum located at the K point, ≈250 meV above the Γ point. A curvature analysis of the Γ and K bands reveals similar hole effective masses compared to the undoped sample (respectively $2.73m_0$ and $1.03m_0$, $m_0$ being the electron mass). The valence band spectra at the K and Γ points are shown in Figures 8c and 8d respectively for the undoped and 5%-doped layers. The spectra are almost identical highlighting the fact that the valence band shift observed by XPS is not related to the $MoSe_2$ layer. Finally we also recorded the band structures of the 2.5% and 7.5% Mn doped $MoSe_2$ monolayers (not shown). They are almost identical to the band structure as the undoped layer at the resolution limit of the setup as if Mn incorporation had no effect on the electronic properties of $MoSe_2$.

## 5. Discussion

Based on our multiscale sample analysis, we draw in this section conclusions about the incorporation of Mn in $MoSe_2$ monolayers. First, RHEED, STEM and STM demonstrated the presence of

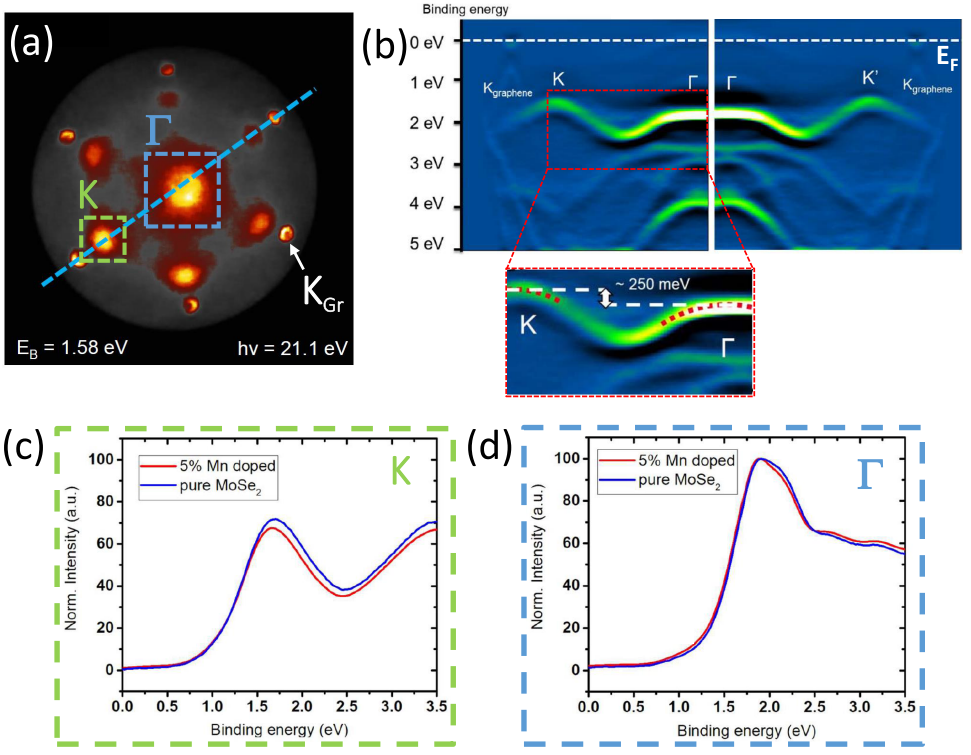


**Figure 8.** Electronic band structure of the $Mo_{0.95}Mn_{0.05}Se_2$ sample. (a) Cut at a binding energy of 1.58 eV. (b) Cut along the blue dashed line in (a) corresponding to the K–Γ–K′ direction. Here, the second-derivative of the band structure is represented. The details around the K and Γ points in the rectangle surrounded with a dashed red line are enlarged in the inset along with the parabola (red dashed line) serving to estimate the hole effective masses. (c) and (d) Integrated intensity of the electronic band structure at the K (green square in (a)) and Γ (blue square in (a)) points respectively for the undoped and doped samples.

MnSe clusters for Mn concentrations above 5%. Below this concentration, Mn atoms are incorporated in the $MoSe_2$ monolayer as shown by XPS measurements. Hence this 5% concentration represents an upper limit for the incorporation of Mn atoms in $MoSe_2$. Then, by electron and X-ray diffraction, we can conclude that the crystal structure of $MoSe_2$ remains unchanged upon Mn doping. The same conclusion can be drawn regarding the electronic structure: the Mo and Se core level spectra in XPS measurements and the electronic band structure measured by *k*-PEEM are very similar to those of bare $MoSe_2$. Those conclusions are confirmed by STEM observations where the inner part of $MoSe_2$ single crystalline grains do not show the presence of Mn atoms (except for one area where we could fortuitously detect one Mn atom substituting Mo). The answer is then given by STM/STS measurements where we clearly see that incorporated Mn atoms tend to diffuse to the edge of the $MoSe_2$ grains leaving their inner part intact.

Therefore, Mn atoms accumulate at grain edges to form an undefined $Mo_xMn_ySe_z$ phase which, at the completion of one monolayer, is located at grain boundaries. The spontaneous decomposition between pure $MoSe_2$ and a Mn-rich phase was also referred to as spinodal nanodecomposition in DMS [6]. In magnetic measurements, it is highly probable that any de-

tected signal on such samples would exclusively come from this Mn-rich phase. Finally, the valence band shift detected upon Mn incorporation in XPS is probably due to the occupation of in-gap states (as shown by STS) or by the presence of the MnSe clusters. In summary, the growth conditions by MBE to obtain high crystalline quality $MoSe_2$ monolayers systematically lead to the segregation of Mn dopants to the grain edges and to the formation of MnSe clusters above 5% when grain edges are saturated. The resulting Mn solubility in $MoSe_2$ is thus extremely low. Lowering the growth temperature would probably limit the diffusion of Mn atoms but would result in poor quality $MoSe_2$ layer since the optimized growth conditions for the epitaxy of $MoSe_2$ on graphene are within a very narrow window for the growth temperature and deposition rates. Mn-doping of $MoSe_2$ by MBE might not be the good strategy to obtain a well-defined $Mo_{1-x}Mn_xSe_2$ diluted magnetic semiconductor. One possible explanation is the absence of stable $MnSe_2$ two-dimensional phase: the 1T-$MnSe_2$ phase, predicted ferromagnetic [40], is thermodynamically unstable. This situation is at odd with vanadium doping because the 1T-$VSe_2$ phase is stable and might be easily incorporated into $MoSe_2$ or $WSe_2$ as recently shown [26]. Moreover, substitutional vanadium doping of $WSe_2$ was recently reported by several groups either theoretically [41] or experimentally [42, 43] showing very promising ferromagnetic properties.

## 6. Conclusion

We have grown $Mo_{1-x}Mn_xSe_2$ monolayers with $x \leq 0.1$ by MBE on graphene using the optimized growth conditions for $MoSe_2$. By using a multiscale characterization approach including in-situ RHEED, X-ray diffraction, STEM, STM/STS, XPS and $k$-PEEM, we could study the incorporation of Mn in $MoSe_2$. The combination of all these techniques allowed us to conclude about the extremely low solubility of Mn in $MoSe_2$. During MBE growth, Mn dopants segregate at the grain edges forming undefined $Mo_xMn_ySe_z$ phase at grain boundaries. The crystal and electronic structure of $MoSe_2$ grains remain unchanged upon Mn doping. Above 5% of Mn, epitaxial cubic MnSe clusters start forming at the surface of the film. Finally, Mn doping of $MoSe_2$ by MBE might not be the most suitable strategy to achieve a diluted $MoSe_2$:Mn magnetic semiconductor.

## Acknowledgments

The authors are supported by the French ANR project MAGICVALLEY through grant ANR-18-CE24-0007. The LANEF framework (no. ANR-10-LABX-51-01) is also acknowledged for its support with mutualized infrastructure. Part of this work was performed on the Platform for NanoCharacterisation (PFNC) of CEA and was supported by the "Recherche Technologique de Base" Program of the French Ministry of Research.

## References

[1] S. A. Wolf, D. D. Awschalom, R. A. Buhrman, J. M. Daughton, S. von Molnár, M. L. Roukes, A. Y. Chtchelkanova, D. M. Treger, "Spintronics: A spin-based electronics vision for the future", *Science* **294** (2001), p. 1488-1495.

[2] H. Ohno, "Making nonmagnetic semiconductors ferromagnetic", *Science* **281** (1998), p. 951-958.

[3] M. Sawicki, D. Chiba, A. Korbecka, Y. Nishitani, J. A. Majewski, F. Matsukura, T. Dietl, H. Ohno, "Experimental probing of the interplay between ferromagnetism and localization in (Ga, Mn)As", *Nat. Phys.* **6** (2010), p. 22-25.

[4] D. Chiba, M. Sawicki, Y. Nishitani, Y. Nakatani, F. Matsukura, H. Ohno, "Magnetization vector manipulation by electric fields", *Nature* **455** (2008), p. 515-518.

[5] L. Chen, S. Yan, P. F. Xu, J. Lu, W. Z. Wang, J. J. Deng, X. Qian, Y. Ji, J. H. Zhaoa, "Low-temperature magnetotransport behaviors of heavily Mn-doped (Ga, Mn)As films with high ferromagnetic transition temperature", *Appl. Phys. Lett.* **95** (2009), article no. 182505.

[6] T. Dietl, K. Sato, T. Fukushima, A. Bonanni, M. Jamet, A. Barski, S. Kuroda, M. Tanaka, P. N. Hai, H. Katayama-Yoshida, "Spinodal nanodecomposition in semiconductors doped with transition metals", *Rev. Mod. Phys.* **87** (2015), p. 1311-1377.

[7] K. F. Mak, C. Lee, J. Hone, J. Shan, T. F. Heinz, "Atomically thin $MoS_2$: A new direct-gap semiconductor", *Phys. Rev. Lett.* **105** (2010), article no. 136805.

[8] B. Radisavljevic, A. Radenovic, J. Brivio, V. Giacometti, A. Kis, "Single-layer $MoS_2$ transistors", *Nat. Nanotechnol.* **6** (2011), p. 147-150.

[9] H. Ohno, A. Shen, F. Matsukura, A. Oiwa, A. Endo, S. Katsumoto, Y. Iye, "(Ga, Mn)As: A new diluted magnetic semiconductor based on GaAs", *Appl. Phys. Lett.* **69** (1996), p. 363-365.

[10] A. Koma, "Van der Waals epitaxy—a new epitaxial growth method for a highly lattice-mismatched system", *Thin Solid Films* **216** (1992), p. 72-76.

[11] M. T. Dau, M. Gay, D. D. Felice, C. Vergnaud, A. Marty, C. Beigné, G. Renaud, O. Renault, P. Mallet *et al.*, "Beyond van der Waals interaction: The case of $MoSe_2$ epitaxially grown on few-layer graphene", *ACS Nano* **12** (2018), p. 2319-2331.

[12] M. T. Dau, C. Vergnaud, A. Marty, C. Beigné, S. Gambarelli, V. Maurel, T. Journot, B. Hyot, T. Guillet, B. Grévin, H. Okuno, M. Jamet, "The valley nernst effect in $WSe_2$", *Nat. Commun.* **10** (2019), article no. 5796.

[13] M. T. Dau, C. Vergnaud, M. Gay, C. J. Alvarez, A. Marty, C. Beigné, D. Jalabert, J.-F. Jacquot, O. Renault, H. Okuno, M. Jamet, "van der Waals epitaxy of Mn-doped $MoSe_2$ on mica", *APL Mater.* **7** (2019), article no. 051111.

[14] C. Vergnaud, M.-T. Dau, B. Grévin, C. Licitra, A. Marty, H. Okuno, M. Jamet, "New approach for the molecular beam epitaxy growth of scalable $WSe_2$ monolayers", *Nanotechnology* **31** (2020), article no. 255602.

[15] S. Vishwanath, X. Liu, S. Rouvimov, L. Basile, N. Lu, A. Azcatl, K. Magno, R. M. Wallace, M. Kim, J.-C. Idrobo, J. K. Furdyna, D. Jena, H. G. Xing, "Controllable growth of layered selenide and telluride heterostructures and superlattices using molecular beam epitaxy", *J. Mater. Res.* **31** (2016), p. 900-910.

[16] C. M.-W., D. Ovchinnikov, S. Lazar, M. Pizzochero, M. B. Whitwick, A. Surrente, M. Baranowski, O. L. Sanchez, P. Gillet, P. Plochocka, O. V. Yazyev, A. Kis, "Highly oriented atomically thin ambipolar $MoSe_2$ grown by molecular beam epitaxy", *ACS Nano* **11** (2017), p. 6355-6361.

[17] R. Mishra, W. Zhou, S. J. Pennycook, S. T. Pantelides, J.-C. Idrobo, "Long-range ferromagnetic ordering in manganese-doped two-dimensional dichalcogenides", *Phys. Rev. B* **88** (2013), article no. 144409.

[18] J. Wang, F. Sun, S. Yang, Y. Li, C. Zhao, M. Xu, Y. Zhang, H. Zeng, "Robust ferromagnetism in Mn-doped $MoS_2$ nanostructures", *Appl. Phys. Lett.* **109** (2016), article no. 092401.

[19] K. Zhang, S. Feng, J. Wang, A. Azcatl, N. Lu, R. Addou, N. Wang, C. Zhou, J. Lerach, V. Bojan, M. J. Kim *et al.*, "Manganese doping of monolayer $MoS_2$: The substrate is critical", *Nano Lett.* **15** (2015), p. 6586-6591.

[20] C. Vergnaud, M. Gay, C. Alvarez, M.-T. Dau, F. Pierre, D. Jalabert, C. Licitra, A. Marty, C. Beigné, B. Grévin, O. Renault, H. Okuno, M. Jamet, "Van der Waals solid phase epitaxy to grow large-area manganese-doped $MoSe_2$ few-layers on $SiO_2$/Si", *2D Mater.* **6** (2019), article no. 035019.

[21] C. J. Alvarez, M. T. Dau, A. Marty, C. Vergnaud, H. L. Poche, P. Pochet, M. Jamet, H. Okuno, "Impact of a van der Waals interface on intrinsic and extrinsic defects in an $MoSe_2$ monolayer", *Nanotechnology* **29** (2018), article no. 425706.

[22] Y. Ma, S. Kolekar, H. C. Diaz, J. Aprojanz, I. Miccoli, C. Tegenkamp, M. Batzill, "Metallic twin grain boundaries embedded in $MoSe_2$ monolayers grown by molecular beam epitaxy", *ACS Nano* **11** (2017), p. 5130-5139.

[23] T. L. Quang, V. Cherkez, K. Nogajewski, M. Potemski, M. T. Dau, M. Jamet, P. Mallet, J.-Y. Veuillen, "Scanning tunneling spectroscopy of van der Waals graphene/semiconductor interfaces: absence of fermi level pinning", *2D Mater.* **4** (2017), article no. 035019.

[24] H. Liu, L. Jiao, F. Yang, Y. Cai, X. Wu, W. Ho, C. Gao, J. Jia, N. Wang, H. Fan, W. Yao, M. Xie, "Dense network of one-dimensional midgap metallic modes in monolayer $MoSe_2$ and their spatial undulations", *Phys. Rev. Lett.* **113** (2014), article no. 066105.

[25] S. Barja, S. Wickenburg, Z.-F. Liu, Y. Zhang, H. Ryu, M. M. Ugeda, Z. Hussain, Z.-X. Shen, S.-K. Mo, E. Wong *et al.*, "Charge density wave order in 1D mirror twin boundaries of single-layer $MoSe_2$", *Nat. Phys.* **12** (2016), p. 751-756.

[26] P. Mallet, F. Chiapello, H. Okuno, H. Boukari, M. Jamet, J.-Y. Veuillen, "Bound hole states associated to individual vanadium atoms incorporated into monolayer $WSe_2$", *Phys. Rev. Lett.* **125** (2020), article no. 036802.

[27] S. Barja, S. Refaely-Abramson, B. Schuler, D. Y. Qiu, A. Pulkin, S. Wickenburg, H. Ryu, M. M. Ugeda, C. Kastl, C. Chen *et al.*, "Identifying substitutional oxygen as a prolific point defect in monolayer transition metal dichalcogenides", *Nat. Commun.* **10** (2019), article no. 3382.

[28] S. Yoshida, Y. Kobayashi, R. Sakurada, S. Mori, Y. Miyata, H. Mogi, T. Koyama, O. Takeuchi, H. Shigekawa, "Microscopic basis for the band engineering of $Mo_{1x}W_xS_2$-based heterojunction", *Sci. Rep.* **5** (2015), article no. 14808.

[29] Y.-H. Chu, L.-H. Wang, S.-Y. Lee, H.-J. Chen, P.-Y. Yang, C. J. Butler, L.-S. Lu, H. Yeh, W.-H. Chang, M.-T. Lin, "Atomic scale depletion region at one dimensional $MoSe_2$–$WSe_2$ heterointerface", *Appl. Phys. Lett.* **113** (2018), article no. 241601.

[30] A. Ramasubramaniam, D. Naveh, "Mn-doped monolayer $MoS_2$: An atomically thin dilute magnetic semiconductor", *Phys. Rev. B* **87** (2013), article no. 195201.

[31] Y. C. Cheng, Q. Y. Zhang, U. Schwingenschlogl, "Valley polarization in magnetically doped single-layer transition-metal dichalcogenides", *Phys. Rev. B* **89** (2014), article no. 155409.
[32] X. Lin, J. Ni, "Charge and magnetic states of Mn-, Fe-, and Co-doped monolayer $MoS_2$", *J. Appl. Phys.* **116** (2014), article no. 044311.
[33] C. Zhang, A. Johnson, C.-L. Hsu, L.-J. Li, C.-K. Shih, "Direct imaging of band profile in single layer $MoS_2$ on graphite: quasiparticle energy gap, metallic edge states, and edge band bending", *Nano Lett.* **14** (2014), p. 2443-2447.
[34] L. Quang, K. Nogajewski, M. Potemski, M. T. Dau, M. Jamet, P. Mallet, J.-Y. Veuillen, "Band-bending induced by charged defects and edges of atomically thin transition metal dichalcogenide films", *2D Mater.* **5** (2018), article no. 035034.
[35] P. Weightman, E. D. Roberts, C. E. Johnson, "$L_{2,3}MM$ auger processes in selenium", *J. Phys. C: Solid State Phys.* **4** (1975), article no. 0550.
[36] M. C. Biesinger, B. P. Payne, A. P. Grosvenor, M. W. M. Lau, A. R. Gerson, R. S. C. Smart, "Resolving surface chemical states in XPS analysis of first row transition metals, oxides and hydroxides: Cr, Mn, Fe, Co and Ni", *Appl. Surf. Sci.* **257** (2011), p. 2717-2730.
[37] J. J. Yeh, I. Lindau, "Atomic subshell photoionization cross sections and asymmetry parameters: $1 \leq Z \leq 103$", *At. Data Nucl. Data Tables* **32** (1985), p. 1-155.
[38] M. Escher, N. Weber, M. Merkel, C. Ziethen, P. Bernhard, G. Schönhense, S. Schmidt, F. Forster, F. Reinert, B. Krömker, D. Funnemann, "NanoESCA: a novel energy filter for imaging X-ray photoemission spectroscopy", *J. Phys.: Condens. Matter* **17** (2005), p. S1329-S1338.
[39] M. Escher, K. Winkler, O. Renault, N. Barrett, "Applications of high lateral and energy resolution imaging XPS with a double hemispherical analyser based spectromicroscope", *J. Elect. Spectr. Relat. Phenom.* **178** (2010), p. 303-316.
[40] M. Kan, S. Adhikarib, Q. Sun, "Ferromagnetism in $MnX_2$ (X = S, Se) monolayers", *Phys. Chem. Chem. Phys.* **16** (2014), p. 4990.
[41] D. L. Duong, S.-G. Kim, Y. H. Lee, "Gate modulation of the long-range magnetic order in a vanadium-doped $WSe_2$ semiconductor", *AIP Adv.* **10** (2020), article no. 065220.
[42] Y. T. H. Pham, M. Liu, V. O. Jimenez, Z. Yu, V. Kalappattil, F. Zhang, K. Wang, T. Williams, M. Terrones, M.-H. Phan, "Tunable ferromagnetism and thermally induced spin flip in vanadium-doped tungsten diselenide monolayers at room temperature", *Adv. Mater.* **32** (2020), article no. 2003607.
[43] S. J. Yun, D. L. Duong, D. M. Ha, K. Singh, T. L. Phan, W. Choi, Y.-M. Kim, Y. H. Lee, "Ferromagnetic order at room temperature in monolayer $WSe_2$ semiconductor via vanadium dopant", *Adv. Sci.* **7** (2020), article no. 1903076.